Scientific Reports

https://doi.org/10.1038/s41598-026-49009-w

Article in Press

Localized heat induces ERK activation and signal propagation in solid tumors

Received: 13 January 2026

Accepted: 12 April 2026

Published online: 30 April 2026

Cite this article as: Taemaitree F., Takano Y., Yamaguchi D. *et al.* Localized heat induces ERK activation and signal propagation in solid tumors. *Sci Rep* (2026). https://doi.org/10.1038/s41598-026-49009-w

Farsai Taemaitree, Yuta Takano, Daisuke Yamaguchi, Kazushi Yamaguchi, Yudai Yamashita, Motosuke Tsutsumi, Chentao Wen, Kohei Otomo, Kenji Hirai, James Hutchison, Indra Zundert, Sandra Krzyzowska, Maria Bravo, Sayuki Hirano, Koutarou D. Kimura, Kazuhiro Aoki, Susana Rocha, Tomomi Nemoto, Beatrice Fortuni & Hiroshi Uji-i

Localized Heat Induces ERK Activation and Signal Propagation in Solid Tumors

Farsai Taemaitree[a,b,c,‡], Yuta Takano[a,d,‡,*], Daisuke Yamaguchi[b], Kazushi Yamaguchi[b], Yudai Yamashita[b], Motosuke Tsutsumi[e,f], Chentao Wen[g,h], Kohei Otomo[e,f,i], Kenji Hirai[a,b], James Hutchison[j], Indra Van Zundert[k], Sandra Krzyzowska[k], Maria Bravo[k,j], Sayuki Hirano[m], Koutarou D Kimura[g], Kazuhiro Aoki[e,l,m], Susana Rocha[k], Tomomi Nemoto[e,f*], Beatrice Fortuni[k*] and Hiroshi Uji-i[a,b,k,n*]

a. *Research Institute for Electronic Science, Hokkaido University, N20, W10, Sapporo 001-0020, Japan.*

b. *Graduate School of Information Science and Technology, Hokkaido University, N14, W9, Sapporo 060-0813, Japan.*

c. *Institute of Multidisciplinary Research for Advanced Materials (IMRAM), Tohoku University, 2–1–1 Katahira, Aoba–Ward, Sendai, 980–8577 Japan*

d. *Graduate School of Environmental Science, Hokkaido University, N10, W5, Sapporo 060-0814, Japan.*

e. *Exploratory Research Center on Life and Living Systems, National Institutes of Natural Sciences, Higashiyama 5-1, Myodaiji, Okazaki, Aichi 444-8787, Japan*

f. *National Institute for Physiological Sciences, National Institutes of Natural Sciences, Higashiyama 5-1, Myodaiji, Okazaki, Aichi 444-8787, Japan.*

g. *Graduate School of Science, Nagoya City University, Nagoya 467-8501, Japan*

h. *RIKEN Center for Biosystems Dynamics Research, Kobe 650-0047, Japan.*

i. *Graduate School of Medicine, Juntendo University, 2-1-1 Hongo, Tokyo 113-8421, Japan*

j. *ARC Centre of Excellence in Exciton Science, School of Chemistry, University of Melbourne, Parkville, VIC 3010, Australia*

k. *Molecular Imaging and Photonics, Department of Chemistry, KU Leuven, Celestijnenlaan 200F, Heverlee 3001, Belgium*

l. *National Institute for Basic Biology, National Institutes of Natural Sciences, Okazaki, Aichi 444-8585, Japan.*

m. *Graduate School of Biostudies, Kyoto University, Sakyo-ku, Kyoto 606-8315, Japan.*

n. *Institute for Integrated Cell-Material Science (WPI-iCeMS), Kyoto University, Yoshida, Sakyo-ku, Kyoto 606-8501, Japan.*

Corresponding Authors: Yuta Takano, tak@es.hokudai.ac.jp, Tomomi Nemoto, tn@nips.ac.jp, Beatrice Fortuni, beatrice.fortuni@kuleuven.be, and Hiroshi Uji-i, hiroshi.ujii@es.hokudai.ac.jp

Footnote: ‡Y.T. and F.T. contributed equally to this work.

Competing interests: The authors declare no conflict of interest.

Classification: MAJOR; PHYSICAL SCIENCES, BIOLOGICAL SCIENCES

Minor; Chemistry, Biophysics and Computational Biology

Keywords: Photothermal therapy, ERK signaling, Tumor Spheroids, Gold nanoparticles.

Abstract

Localized plasmonic heating by metallic nanoparticles offers a promising strategy to destroy cancer cells through controlled thermal stress. However, how cells sense and respond to microscale temperature variations within complex tissue environments remains unclear. Here, the problem that is being addressed is how plasmon-induced local heating reshapes intracellular signaling and cell fate within tumor spheroids, focusing on the extracellular signal-regulated kinase (ERK) pathway. HeLa spheroids expressing a FRET-based ERK biosensor were subjected to defined photothermal stimuli using gold nanostars as nanoscale heat sources, while ERK activity was tracked with a deep-learning algorithm (3DeeCellTracker). Local heating triggered marked alterations in ERK signaling dynamics compared to spontaneous activity, including changes in activation frequency, timing, and duration. Remarkably, heat-induced ERK activation spread across neighboring cells, revealing thermally mediated intercellular propagation. Quantitative analysis further showed that temperature elevation modulates cell death and division in a power-dependent manner. These results uncover how nanoscale heat generation governs signaling networks and collective cellular behavior, providing a mechanistic framework to understand and optimize heat-based cancer treatment strategies.

Introduction

Localized heat generation at the micro- and nanoscale underpins emerging strategies to selectively eliminate cancer cells through controlled thermal stress.[1,2] However, how cells sense and respond to such microscale temperature fluctuations within complex tissue environments remains unknown. Rapid progress has been made in the design of photothermal nanoagents,[3,4] but molecular and cellular mechanisms activated by localized heating are still poorly understood. Bridging this knowledge gap is essential for advancing next-generation heat-based cancer treatments and for developing a deeper understanding of how thermal cues influence cellular signaling and behavior.

One effective method for exploring cellular responses to stress is by examining extracellular signal-regulated kinase (ERK) activity. ERK belongs to the family of mitogen-activated protein kinases (MAPK), which play a crucial role in pathways that transmit extracellular signals to their intracellular targets,[5–8] thereby regulating numerous biological processes including cell proliferation and differentiation, cellular adaptation/survival,[9] and apoptosis.[10,11] Therefore, monitoring the activation of ERK signaling pathways holds promise for gaining valuable insights into how cells adapt and respond to localized thermal stress at a single-cell level.

At the same time, the implementation of advanced three-dimensional (3D) tumor platforms represents an innovative approach to better replicate the tumor microenvironment and improve the translational relevance of preclinical studies. Among various 3D cancer models, spheroids effectively mimic the intricate architecture of cancerous tissues and their microenvironment, displaying cell-to-cell interactions, as well as intercellular signaling.[12–14]

Here, we investigate how plasmon-induced local heating modulates intracellular signaling and fate decisions within 3D tumor spheroids. Using HeLa cells expressing a FRET-based ERK biosensor and deep-learning tracking (3DeeCellTracker), we mapped spatiotemporal ERK dynamics following controlled photothermal stimulation by gold nanostars (AuNSs). This integrated approach offers several advantages: (i) allowing for precise control of laser intensity to regulate heat generation by AuNSs, (ii) facilitating high-resolution image acquisition in multicellular 3D cell systems, and (iii) enabling single-cell level analysis of over 1000 cells simultaneously. The results reveal how nanoscale thermal gradients reshape collective cellular behavior, providing a mechanistic understanding of heat–cell interactions towards the rational design of next-generation heat-based cancer treatments.

Methods

General

Absorption spectra were recorded using a UV-Vis spectrophotometer (V-730, JASCO, Japan). Dynamic Light Scattering (DLS) and zeta potential measurements were conducted at room temperature in Milli-Q water using Zetasizer Nano ZS (Malvern Panalytical Ltd., U.K.). All chemicals and solvents used in this study were of analytical grade and used as received unless otherwise stated.

Synthesis and characterization of Cysteamine-coated AuNS (AuNS-Cys)

Synthesis: a gold nanostar (AuNS) colloidal solution was prepared according to previous reports.[15] Briefly, 3 mL of 1.0% citric acid solution was added to 20 mL of boiling 1.0 mM tetrachloroauric(III) acid trihydrate ($HAuCl_4$) aqueous solution and stirred for 15 min at 110°C. The dispersion was allowed to cool to room temperature and was subsequently stored at 4°C for 24 h. Next, 10 mL of 0.25 mM $HAuCl_4$ aqueous solution, 100 μL of 1.0 M HCl, and 100 μL of the gold colloid dispersion were mixed and stirred. 100 μL of 3.0 mM silver nitrate ($AgNO_3$) aqueous solution and 100 μL of 100 mM ascorbic acid (AA) solution were added simultaneously to the mixture at room temperature. Immediately after the mixture turned blue, it was centrifuged at 3000 × g for 15 min to stop nucleation, then the supernatant was removed. Milli-Q water was added and a dispersed AuNS solution was obtained after sonication for 5 min.

The AuNS dispersion (1.0 mg/mL) was rapidly mixed with 80 mM cysteamine aqueous solution in equal volumes, sonicated for 30 min under light shielding, centrifuged at 3000 × g for 10 min, and washed with Milli-Q water. This washing process was repeated three times to remove excess cysteamine and obtain cysteamine-coated AuNS (AuNS-Cys) dispersed in Milli-Q water at 1.0 mg/mL concentration.

STEM characterization: 10 μL of AuNS-Cys dispersion was dropped onto a copper mesh grid (collodion film-applied mesh, Nissin EM Co., Ltd.), dried under vacuum for at least 30 min, and observed using a HITACHI HD-2000 (Hitachi, Japan) with an acceleration voltage of 200 kV. Images were acquired in multiple fields of view for one grid and used to measure particle size. Several fields of view were measured and the particle diameter was determined as the maximum Euclidean distance between any two points on the AuNS-Cys perimeter. The particle core diameter was the darkest area from the shading of the STEM image. The results showed that the mean particle diameter ± standard deviation (SD) was 101.3 ± 15.0 nm (n = 131) and the mean core diameter was 37.8 ± 6.5 nm (n = 131).

Stability in biological media: The stability of AuNS-Cys was evaluated in cell lysate prepared using Cell Lysis Buffer M (Wako, Japan), and in Dulbecco's modified Eagle's minimal essential medium (DMEM, Wako, Japan) supplemented with 10% fetal bovine serum (FBS, Gibco, USA). In brief, 10 μL of AuNS-Cys dispersion was added to 990 μL of each biological medium and incubated at 37°C for 24 h. The resulting dispersion solutions were then deposited onto copper mesh grid and dried for STEM observation.

Evaluation of local heating effects

8 uL of the AuNS-Cys dispersion was dropped onto a cover glass and spin-coated at 30 rps for 30 s. The samples were then dried on a hotplate at 90°C for 30 s. A polydimethylsiloxane (PDMS) framework was pasted onto the cover glass to function as a chamber for poly (N-isopropylacrylamide) (PNIPAM) solution. Next, 40 μL of a solution of water and 1,4-dioxane (1:1 v/v) containing 5 mg/mL PNIPAM (Sigma-Aldrich, Japan) was added to the PDMS framework, covering the spin-coated AuNS-Cys. Plasmonic heating effects were observed using an inverted optical microscope (Ti-U, NIKON, Japan) with an 808 nm CW laser, 12.5 mW (1.2 MW cm^{-2}). The laser beam was reflected by a dichroic mirror and focused onto the sample using an objective lens (PlanFluo x60, NA 0.85, Nikon). To eliminate Rayleigh scattering, a long-pass filter (ET750SP-2P8, Chroma, USA) was placed in front of the camera when using the 850 nm fs laser. Additionally, a long-pass filter (ET500LP, Chroma) was placed in front of the camera to cut off the light of the 850 nm harmonic. Bright-field images from the microscope illumination were analyzed by software (Hokawo/Hamamatsu Photonics, Japan) using a CCD camera (ImagEM, Hamamatsu Photonics). Laser power measurements were performed at the objective lens using a power meter (THORLABS, USA) to determine the power of the laser incident on the sample.

Culturing HeLa cells with a stable expression of EKAREV-NLS (#T-HeLa)

HeLa cells were purchased from Riken Cell Bank (RRID: CVCL_0030, RCB0007, certified as mycoplasma-free and authenticated by using STR profiling). For the real-time observation of ERK activity in individual cells, a fluorescence resonance energy transfer (FRET) sensor protein, EKAREV-NLS, was stably expressed in HeLa cells (#T-HeLa).[16] Briefly, plasmids with EKAREV-NLS construct developed previously[17] and plasmid with PiggyBac transposon were introduced into cells via lipofection (Lipofectamine, Thermo Fischer Scientific, USA) at 3 to 1 ratio. After lipofection, the cells were cultured in the presence of 10 mg/mL blasticidin (Invivo Gen, USA) to select transfected cells. Cells stably expressing EKAREV-NLS were maintained and passaged in Dulbecco's modified Eagle's minimal essential medium (DMEM, Wako, Japan) supplemented with 10% fetal bovine serum (FBS, Gibco, USA) and 1% penicillin/streptavidin (P/S, Wako, Japan). Cells were cultured at 37°C in 5% CO_2/air. Cell passages were performed at 80-90% confluency using trypsin.

Dark cytotoxicity assay

The cytotoxicity of AuNS-Cys was evaluated by measuring the number of viable cells with a cell counter. In detail, the cells were seeded in 35 mm glass bottom dishes at a density of 2.0 × 10^5 cells per dish with 1 mL cell culture medium and incubated at 37°C for 24 h under 5% CO_2. The next day, after confirming cell adhesion to the bottom of the dish, 50 μL of AuNS-Cys solution (1.0 mg/mL) was added and incubated for 10 min. After incubation, the cells were washed with Dulbecco's Phosphate-Buffered Saline (D-PBS (−), Wako, Japan) and incubated for 48 h at 37°C. Next, the number of viable cells was counted by staining dead cells with trypan blue. Each test was performed in triplicate.

Preparation of spheroids of #T-HeLa

A suspension of #T-HeLa cell culture medium (200 μL) containing 3600 cells was dropped into a 96-well plate designated for spheroid preparation (MS-9096U; Sumitomo Bakelite, Japan). The plates were then covered with lids and incubated for 48 h at 37°C in 5% CO_2. Spheroid formation was monitored using an optical microscope.

3D-imaging of the spheroids of #T-HeLa by a two-photon laser microscope

AuNS-Cys solution was added to each well of a 96-well plate (MS-9096U) filled with #T-HeLa spheroids and gently pipetted, followed by incubation for 10 min at 37°C and 5% CO_2. The spheroids were removed from the wells and submerged in 3 mL of D-PBS (−) solution to remove excess AuNS-Cys. The spheroids were then transferred to a 35 mm glass bottom dish coated with poly-lysine, and 2.0 mL of culture medium was added. Typically, the dose concentration of the AuNS-Cys dispersion solution was 25 μg/mL for the experiments at high concentration of AuNS-Cys and 2.5 ng/mL for those at low concentration of AuNS-Cys.

The sample was then imaged using a multi-photon excitation inverted microscope (A1R-MP, Nikon, Japan) equipped with a silicone oil immersion objective lens (CFI Plan Apochromat Lambda S 25XC Sil, NA 1.05, SIL, Nikon, Japan). Correction rings were aligned to maximize the fluorescence intensity of the samples. A wavelength-tunable Titanium Sapphire (Ti-Sa) laser (850 nm, 120 fs, 80 MHz) was used to excite cyan fluorescent protein (CFP), yellow fluorescent protein (YFP), and AuNS-Cys. The excitation laser power densities used were 0.3 MW cm^{-2} (normal conditions), 4.9 MW cm^{-2} (moderate conditions), and 14.6 MW cm^{-2} (high-intensity conditions). Note that the excitation wavelength of 850 nm can simultaneously realize photo-thermal local stimulation by AuNS-Cys and imaging of ERK activity through two-photon excitation. Dichroic mirrors were used to detect the fluorescence and photoluminescence (PL) from the FRET probe and AuNS-Cys, respectively. 400-492 nm

fluorescence was acquired for CH1 (CFP), 500-550 nm for CH2 (YFP), and 601-657 nm for CH3 (AuNS-Cys, although detectable in all three channels).

The acquired area was 512 × 512 pixels (related to 450 × 450 μm^2) in the xy plane. In the z-direction, imaging was performed from the cover glass surface (the bottom of the spheroid) to the center, which is typically approximately 100 μm in height. During measurements, a stage incubator was used to maintain the extracellular environment at 37°C and 5% CO_2. The cells were placed on the stage for 30 min prior to imaging for stabilization.

For evaluating the heat-induced therapeutic efficacy in spheroids, an aqueous solution of Sulforhodamine B (SRB; Molecular Probes) was added to the spheroids at a concentration of 0.5 mM, 30 min before imaging. SRB was detected under 850 nm excitation wavelength, and the fluorescence was measured at 570–650 nm.[18,19]

Image analysis of the spheroids of #T-HeLa

Changes in ERK activity were visualized as ratiometric images obtained using ImageJ-Fiji.[20] First, background signals from the CFP and YFP were eliminated by automatic thresholding. For each image, the fluorescence intensity of the YFP channel was divided by that of the CFP channel, obtaining ratiometric images representing the FRET efficiency. A color bar was added to each image, indicating the magnitude of FRET efficiency, which is in turn associable with the ERK activity.

The 3DeeCellTracker[21,22] was employed to extract changes in FRET efficiency for each cell within a cancer spheroid. A deep neural network, 3D U-Net[23], was trained using one or a few 3D raw images along with their corresponding annotations of the cell regions. The trained network was then used to detect and segment the cells in a series of 3D images. Another neural network, FFN[22], was used to track the dynamic positions of cells. From detection to tracking, the process demonstrated an accuracy of 97.6 ± 1.9% (n = 3) in the present cases.

The data on changes in FRET efficiency from the cell nuclei were further processed to extract information on the timing of ERK activity. Initially, a linear de-trending process was applied to the FRET efficiency data from individual cell nuclei to remove any linear trends, and information on the timing and frequency of such activity was then extracted. ERK activation was defined as FRET efficiency exceeding the mean of the control condition + 2 standard deviations (SD). This threshold was selected to identify signals significantly above baseline variability and to discriminate activation events from background fluctuations. The distribution of baseline FRET efficiencies in control cells was evaluated by histogram analysis

and found to be approximately normal (Figure S1), supporting the use of this threshold. FRET signals were analyzed at the single-cell level, with the YFP/CFP ratio normalized to the baseline value of each individual cell prior to stimulation, enabling comparison of ERK activity dynamics across cells. Photobleaching correction was not applied, as imaging was performed using short acquisition times and identical laser settings for all conditions, thereby minimizing potential bleaching effects.

Results and discussion

Characterization of Gold Nanostars and their photothermal properties.

Gold nanostars (AuNSs) were chosen as photothermal transducers because of their characteristic plasmonic band in the near-infrared (NIR) light region (~850 nm) and their excellent photothermal conversion efficiency (PCE).[15] They also exhibit an intrinsic photoluminescence (PL) under two-photon excitation[24], which enables their direct observation with fluorescent microscopy.

Surfactant-free AuNSs were synthesized via seed-mediated growth, as previously reported.[15] Immediately after nanostar formation, cysteamine was added as a stabilizing agent, resulting in positively charged nanoparticles at neutral pH, due to the protonated amine groups.[25] Cysteamine is a biocompatible coating that promotes interaction with the negatively charged cell membrane, thereby enhancing cellular uptake.[26] The change in surface charge following cysteamine functionalization was evaluated by zeta potential measurements. The obtained values for AuNS and AuNS-Cys in deionized water were -40.4 ± 4.9 mV and +19.5 ± 5.1 mV, respectively (Figure 1A), confirming the positive shift in surface charge upon functionalization. Importantly, the as-synthesized AuNS without cysteamine are not colloidally stable and rapidly aggregate within minutes after formation. For this reason, the zeta potential of the surfactant-free AuNSs was measured immediately after nanostar formation, when the reaction solution turns blue, and before visible aggregation occurs. The star-shaped morphology of AuNS-Cys was confirmed by Scanning Transmission Electron Microscopy (STEM) (Figure 1B) and their average diameter was estimated to be ~100 nm (Figure S2). UV-

VIS spectroscopy revealed a typical extinction spectrum of star-shaped NPs, characterized by a very broad plasmonic band localized in the NIR region, with a peak at 890 nm (Figure 1C).[27] To evaluate nanoparticle stability in biological media, AuNS–Cys were incubated in cell lysate and cell culture medium for 24 h (Figure S3). TEM images obtained after incubation showed no observable changes in nanoparticle morphology compared with AuNS–Cys dispersed in water, indicating that the nanostars maintain their characteristic shape and remain stable under these biological conditions.

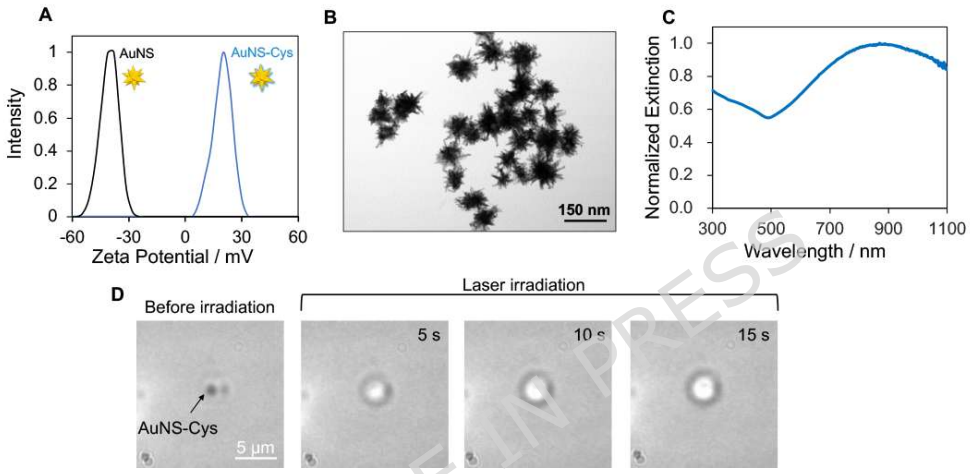

Figure 1. Characterization of AuNS-Cys. (A) Zeta-potential profiles of AuNS (black) and AuNS-Cys (blue). (B) STEM image of AuNS-Cys. (C) Extinction spectrum of AuNS-Cys in water. (D) Thermally induced phase separation in PNIPAM aqueous solution upon photothermal conversion of AuNS-Cys.

The local heating effect of AuNS-Cys was verified by inducing the phase separation in the aqueous solution of a thermoresponsive polymer, poly(N-isopropylacrylamide) (PNIPAM). PNIPAM is known to exhibit a lower critical solution temperature (LCST) of approximately 45°C when dissolved in a 1:1 (v/v) mixture of water and dioxane.[28] To demonstrate the photothermal effect, AuNS-Cys were mixed with a 5 mg/mL PNIPAM solution in 1:1 (v/v) water:dioxane and irradiated with 808 nm excitation. After 5 s of irradiation focused on AuNS-Cys, phase separation was observed, appearing as bubble formation around the AuNSs (Figure 1D). The phase separation continued to enlarge over 15 s of irradiation, indicating that plasmon-induced heating from the AuNS raised the temperature of their surroundings to at

least 45°C within a few seconds of NIR irradiation. This phase-separation assay was used as an experimental indicator of photothermal heating, confirming that laser irradiation of AuNSs can increase the local temperature above the LCST (~45°C). This temperature range is biologically relevant, as temperatures exceeding ~45°C are known to induce irreversible cellular damage. The efficiency of AuNS photothermal conversion was then calculated by previously reported methods[29] and estimated to be 33.7% (details of the calculation are reported in the SI and Figure S4). This value is within the range commonly reported for high-performing plasmonic photothermal materials.[30] Because the irradiation conditions used for the PCE experiment differ substantially from those employed during biological imaging experiments presented later in the manuscript, the PCE measurements serve as a qualitative confirmation of the photothermal response of the AuNSs rather than a direct estimation of the temperature reached inside the spheroids. The phase separation of PNIPAM aqueous solution and the high estimated conversion efficiency indicate that AuNSs can efficiently generate heat upon NIR excitation and can therefore be applied for studying the cellular response to heat in 3D cancer models.

Monitoring ERK activity in 3D cancer spheroids using FRET sensor proteins.

In order to explore the cellular response to localized heat in tumors, real-time monitoring of ERK activity was performed in spheroids upon plasmonic-induced heat by AuNS-Cys. ERK activation was tracked by encoding a previously reported FRET-based biosensor for ERK activity (EKAREV-NLS)[17] in HeLa cells prior to forming spheroids. The EKAREV-NLS sensor includes a FRET donor-acceptor pair (a cyan-emitting protein, CFP, and a yellow-emitting protein, YFP), a sensory domain in between the two fluorescent proteins which is susceptible to phosphorylation, and a ligand domain separated by a flexible linker. Upon perceiving stress-induced phosphorylation, the sensory domain binds to its ligand domain. This interaction results in a conformational change, bringing the two fluorescent proteins closer together, thereby increasing the rate of FRET events (Figure 2A).[17] By observing the change in FRET efficiency as intensity ratio between the acceptor and the donor (YFP/CFP), the ERK activity can be estimated.[31] The modified cells are designated as #T-HeLa cells in this study and were used to form 3D tumor spheroids in a low attachment 96-well plate.

To verify the successful expression of the ERK FRET sensor in #T-HeLa cells and to evaluate the influence of two-photon imaging on #T-HeLa, steady-state ERK activity in #T-

HeLa spheroids was monitored using two-photon fluorescence microscopy. The fluorescence signals of both fluorescent proteins of the sensor, CFP and YFP, were clearly detected when the donor was excited (Figure 2B-C, respectively), indicating the successful expression of the sensor and the occurrence of FRET. The FRET efficiency variations, corresponding to different levels of ERK activity, were analyzed using YFP/CFP ratiometric imaging (Figure 2D). In the ratiometric images, a high YFP/CFP ratio, with cells appearing orange-to-red, indicates high ERK activity, whereas a low YFP/CFP ratio, with cells observed in green, reflects low ERK activity. Figure 2D shows that in a NP-free spheroid, during the scanning, most cells exhibited low ERK activity, appearing in green. Interestingly, a small ratio of cells within the spheroid was observed in orange-red, indicative of ERK activation. These results align with recent studies reporting that spontaneous activation or propagation from neighboring cells can result in sporadic pulses of ERK activity.[6,32] These experiments confirm that the proposed method enables the visualization of FRET efficiencies in individual cells within a spheroid, thereby allowing for precise monitoring of the ERK signaling activity in a 3D tumor structure at the single-cell level.

To accumulate AuNS-Cys into #T-HeLa spheroids, AuNS-Cys were added to the spheroid-containing medium at a final concentration of 25 μg/mL and incubated for 10 min. Note that dark cytotoxicity assays (Figure S5) confirmed that AuNS-Cys (25 μg/mL) had no significant impact on cell viability after 48 h without laser irradiation. The particles accumulation into the spheroids was verified by fluorescence imaging: AuNS-Cys were visualized by their intrinsic PL upon 850 nm two photon excitation,[15] whereas cells were observed though CFP and YFP emission. Confocal fluorescence images revealed that, after 10 min incubation, AuNS-Cys were primarily localized in the peripheral layer of the spheroid, with some adhering to the cell membrane and others being internalized (Figure 2E). The efficient interaction between AuNS-Cys and the cells was attributed to the cysteamine coating. The positive surface charge of AuNS-Cys, acquired through cysteamine functionalization, facilitates electrostatic interactions with the negatively charged cell membrane[33], thereby enhancing NP uptake.[34] This data indicates that AuNS-Cys were successfully accumulated in #T-HeLa spheroids and can therefore be used for studying the effect of plasmonic-induced heat on ERK activity in spheroids over time.

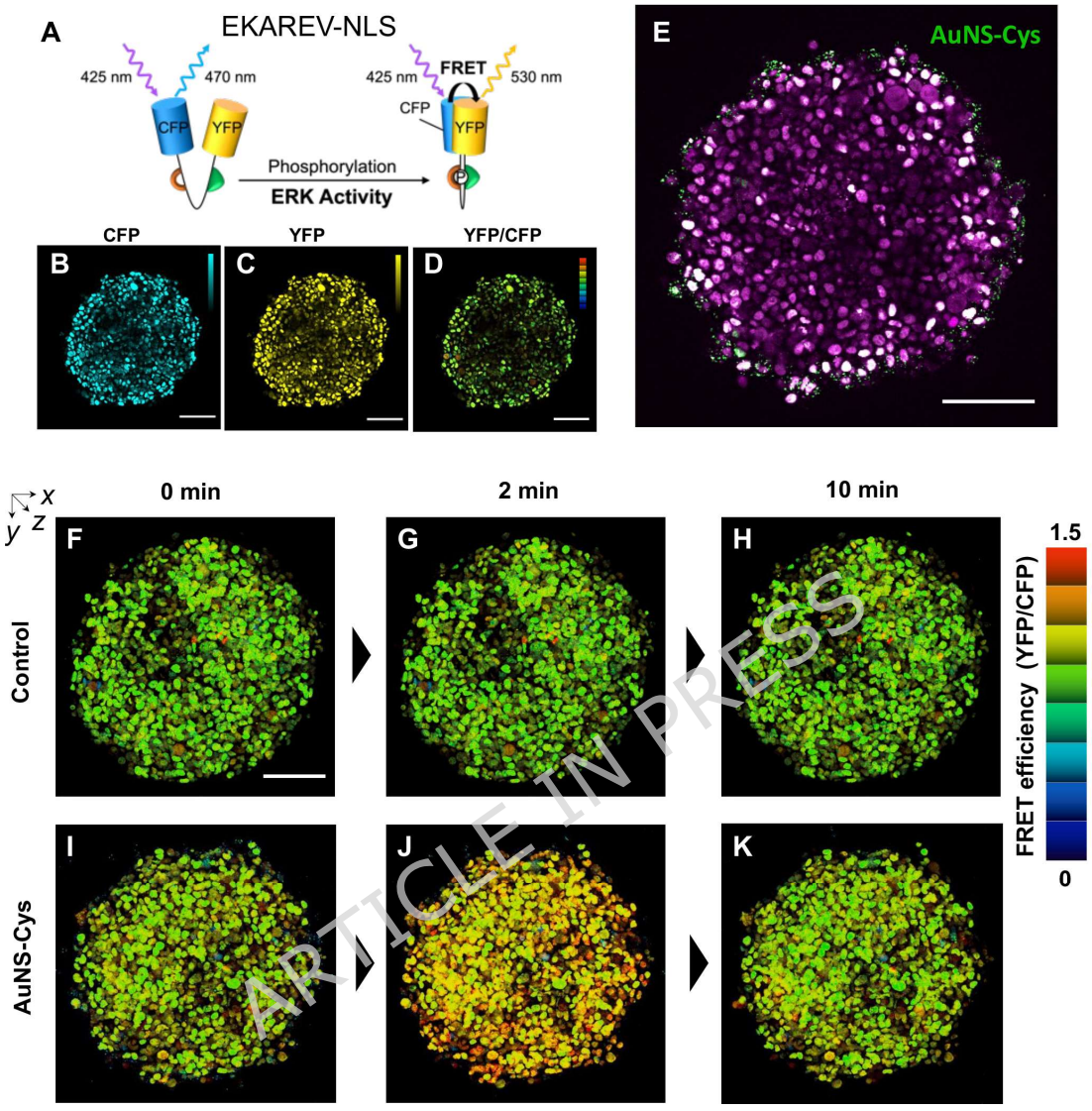

Figure 2. Schematic representation of the FRET biosensor (EKAREV-NLS) structure and activation mechanism (A). xy fluorescence images extracted from z-stacks of EKAREV-NLS expressing HeLa (#T-HeLa) spheroids at 100 µm depth from the spheroid surface displaying CFP and YFP emission (B-C, respectively), upon two-photon donor excitation at 850 nm. YFP/CFP ratiometric images indicating the FRET efficiency corresponding to the ERK activity (D, color bar YFP/CFP: 0-1.5). xy fluorescence images extracted from a z-stack of a #T-HeLa spheroid after 10 min of incubation with AuNS-Cys upon two-photon excitation at 850 nm (E): cells observed in magenta (YFP emission), whereas the AuNS-Cys photoluminescence is displayed in green (CFP emission was also detected in the green channel with the CFP and YFP

overlap appearing in white). Ratiometric maximum intensity z-projections of #T-HeLa spheroids as control (F-H), and of #T-HeLa spheroids incubated with AuNS-Cys (I-K) at 0 min (first scan, F and I, respectively), after 2 min from the first scan (G and J, respectively) and after 10 min from the first scan (H and K, respectively) with 850 nm two-photon excitation (scale bar: 100 μm).

To monitor the spontaneous ERK activity in #T-HeLa spheroids over time without nanoparticles (control), fluorescence scans of a selected focal plane at 100 μm from the spheroid surface were performed at intervals of 2 min for 2 h. Ratiometric fluorescence images at 0, 2 and 10 min are reported as exhibiting the most significant changes (Figure 2F-H, respectively). In agrement with the data shown in Figure 2D, the majority of cells were inactive over the 10-min interval, appearing in green, while a small proportion of active cells were observed in orange or red. This activity pattern remained stable over time, with the same cells exhibiting high ERK activity throughout the 10-min period.

In order to evaluate the effect of plasmon-induced heat on the spontaneous ERK activity observed in the control, the same experiment was repeated after incubation with AuNS-Cys. Ratiometric fluorescence imaging revealed that some cells exhibited signs of activation - appearing yellow - already during the first scan, immediately following AuNS-Cys irradiation (Figure 2I). This differed markedly from the control, which remained predominatly green (Figure 2F), indicating minimal activation. The results suggest that an immediate heat generation may have initiated ERK activation shortly after irradiation. The plasmon-induced heat effect became much more pronounced 2 min after the initial irradiation (Figure 2J), evidenced by a significant increase in both ERK-activation, reflected by the orange-to-red shift in FRET efficiency, and percentage of ERK-active cells. Notably, by 10 min post-irradiation, most cells reverted to their initial ERK-inactive state (Figure 2K), with FRET efficiency levels in yellow-to-green. This dynamic response highlights the transient nature of the ERK activation induced by plasmonic heating. Previous studies have reported inhibition of the MAPK/ERK pathway in the presence of gold nanoparticles; however, these findings predominantly involve small, spherical nanoparticles (~20 nm).[35–38] In contrast, the nanoparticles used in this study are AuNSs larger than 100 nm, which differ substantially in both size and morphology. These differences may explain why no ERK inhibition was observed in

our system, where ERK activation occurred after AuNS–Cys treatment and laser irradiation.

In this study, the use of AuNS-Cys as thermal transducers enabled the delivery of a single, non-reproducible thermal stimulus. Upon irradiation with fs-pulsed laser light, AuNS-Cys likely underwent morphological changes,[39] causing a shift in their plasmonic band and reducing their PCE. This was evidenced by a significant decrease in PL intensity after the initial scans (Figure S6) and confirmed by the PNIPAM phase separation assay, which could not be repeated using the same AuNS-Cys after the first irradiation. These observations indicate that plasmon-induced heating is primarily a one-time event, as structural changes in the nanostars prevent reproducible plasmon-mediated heating upon subsequent irradiation.

These data demonstrate that plasmon-induced heating elicits rapid and robust activation of ERK in tumor spheroids, which is transient, as most cells revert to an ERK-inactive state within 10 min.

3DeeCellTracker analysis of ERK activity in 3D spheroids at single cell-level.

To evaluate the timing and duration of ERK activation at the single-cell level within spheroids, fluorescence imaging data were analyzed using 3DeeCellTracker, an automatic deep-learning program developed by our research group. This tool integrates 3D U-Net[23] and FFN[22] networks trained on relevant datasets, enabling highly accurate (97.6 ± 1.9%) cell nucleus detection and tracking with minimal parameter adjustments. Cell nuclei were identified from YFP fluorescence using 3D U-Net + watershed[40], and their positions were predicted over time for tracking. The fluorescence intensities of CFP and YFP were then extracted from each tracked cell to calculate the FRET efficiency (YFP/CFP). Using 3DeeCellTracker, over 1300 cells were simultaneously tracked for 120 min, providing robust insights into ERK activation dynamics. The resulting data was visualized as raster plots, illustrating the temporal dynamics of the ERK activation in individual cells within the spheroid, for both control (Figure 3A) and AuNS-Cys-induced heat (Figure 3C). Cells with high FRET efficiencies, defined as values exceeding the mean of the control + 2 standard deviations (SD), were classified as ERK-active using descriptive statistical threshold. These cells are represented as black lines in the plots, where each line corresponds to a 2-min duration. These raster plots corroborate the patterns observed in the fluorescence images: the control exhibited random ERK activation events, with black

lines appearing sporadically across different cells over the 120-min interval, while the AuNS-Cys-induced heat triggered a rapid, synchronized ERK activation in the majority of cells, evidenced by densely aligned black lines within the first few minutes post-irradiation.

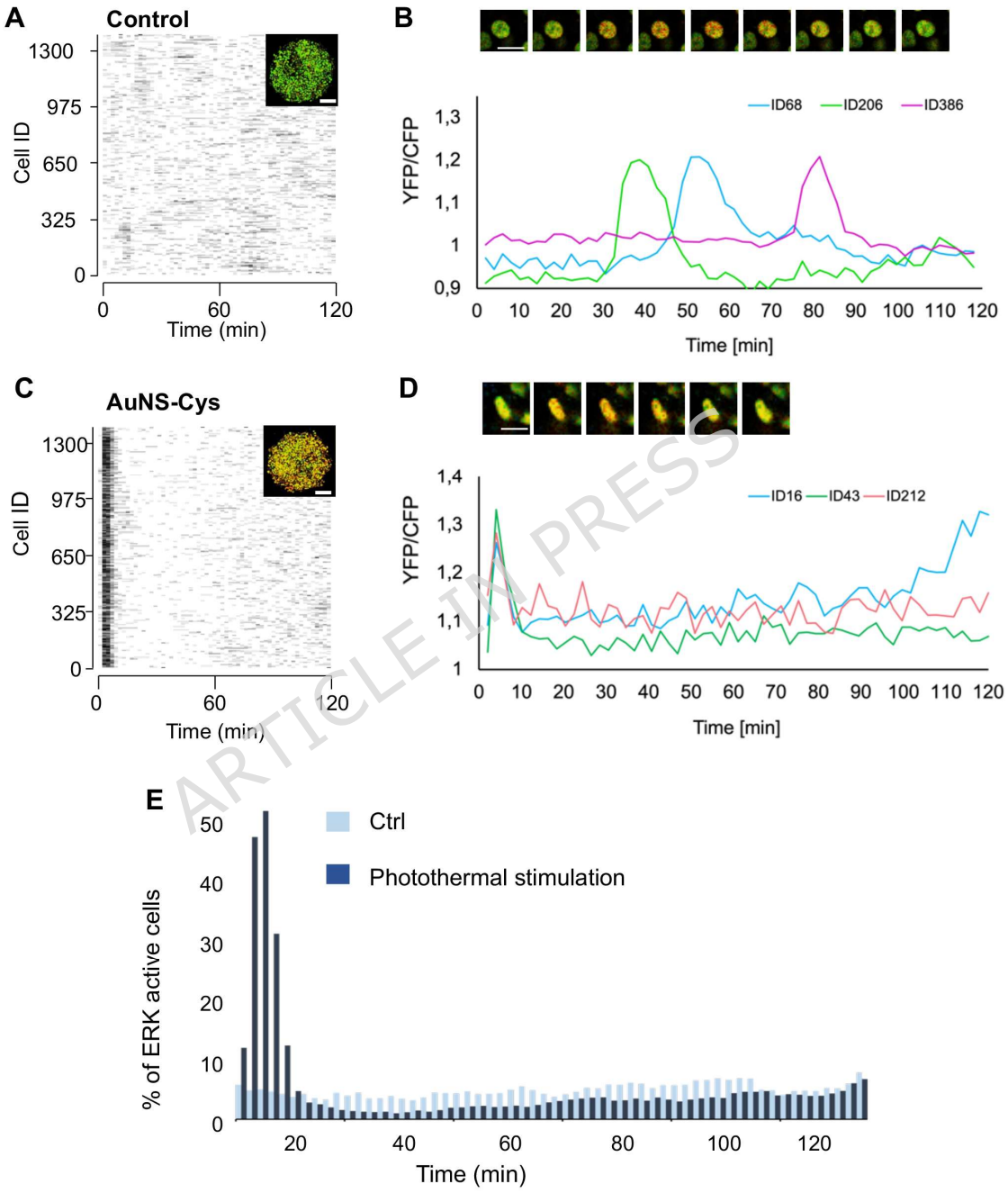

Figure 3. 3DeeCellTracker analysis. Raster plots showing the timing of ERK activation in single cells as a function of time in the control (A) and upon AuNS-Cys-induced photothermal stimuli (C), with insets showing the respective ratiometric image of the spheroid captured at 2-min intervals (scale bar: 100 μm). The black horizontal

lines indicate the ERK-activated state, determined by the FRET efficiency of YFP/CFP exceeding the mean of the control +2 SD, and the duration of each back line is 2 min. A total of n = 1365 cells were analyzed for the control spheroid and n = 1378 cells for the AuNS-treated spheroid. FRET efficiency as YFP/CFP over time of 3 individual cells selected within the spheroids reported in Figure 2F-H for the control (B) and Figure 2I-K for the AuNS-Cys-induced heat condition (D). Insets show ratiometric images of a single representative cell per condition captured at 2-min intervals (scale bar: 20 μm). Percentage of ERK-active cells as a function of time (E) for the control (cyan) and for AuNS-Cys-induced heat condition (dark-blue), obtained from A and C, respectively.

To further characterize the dynamics of ERK activation, FRET efficiency as YFP/CFP over time of three representative cells from control spheroid and spheroid with AuNS-Cys was analyzed (Figures 3B and D, respectively). In the control, spontaneous ERK pulses appeared as broader peaks with durations of 20.0 ± 2.0 min, distributed randomly over the 120-min interval (Figure 3B). In contrast, heat-induced ERK activation displayed sharp peaks of shorter duration (9.3 ± 3.1 min) that were consistently localized within the first few minutes following AuNS-Cys irradiation (Figure 3D). These findings demonstrate that plasmon-induced photothermal effects rapidly cause synchronized ERK activation in the majority of cells and reveal that heat-stimulated ERK activity is significantly shorter in duration than the spontaneous ERK activity in unperturbed cells. This unprecedented insight is essential for understanding and predicting heat-induced cellular responses in solid tumors, as the timing and duration of ERK activation are critical determinants of key cellular processes, including proliferation, differentiation, and apoptosis.[10,41]

From the raster plots, the percentage of ERK-active cells in the control and following plasmon-induced heat was calculated and compared over time (Figure 3E). The basal ERK activity was detected in 3.9 ± 0.6% of cells in the control group. This low activity is comparable to that observed in 2D cell monolayers nearing confluency, where ERK activity diminishes as cells experience contact inhibition of growth - a regulatory mechanism that controls proliferation.[6]

In contrast, the transient increase in ERK activity observed within a few minutes after AuNS-Cys irradiation occurred in 53.7 ± 11.0% of the spheroid cells. Interestingly, 15 min after the initial activation, the cellular ERK activity significantly dropped, resulting in a percentage of

activation lower than that of the control. After 95 min, ERK activity returned to levels comparable to the control, indicating a transient suspension of ERK activity following plasmon-induced heat. Two mechanisms could explain this phenomenon: (1) temporary cell inactivation caused by photothermal stimuli, as protein denaturation and cell inactivation are known to occur when tissue temperatures reach 42°C,[42] or (2) negative feedback suppressing ERK activity in the Ras/ERK or MEK/ERK pathways triggered by local photothermal stimulation.[43,44] Although further investigations are required to confirm these hypotheses, this study provides unique direct observations of ERK activity dynamics in response to local heat in a spheroid over time.

ERK activation and signal propagation.

To investigate the intercellular propagation underlying ERK activation in response to local photothermal stimuli, the experiments were repeated using a 10 times lower concentration of AuNS-Cys (2.5 ng/mL). This adjustment ensured that only a few cells within the spheroid interacted with AuNS-Cys, allowing for the analysis of ERK activation in neighboring cells that were not in direct contact with AuNS-Cys (Figure 4). Fluorescence ratiometric images at the first scan (0 min) showed a uniformly low ERK activity state (with cells in green) and confirmed that only a few AuNS-Cys accumulated in the spheroid, as indicated by white arrows in Figure 4A. Two min after the initial scan, only cells in the surrounding area of AuNS-Cys (white squares, Figure 4B) showed remarkable ERK activation, appearing orange-red, while in the rest of the spheroid, the ERK activation level remained stable (in green).

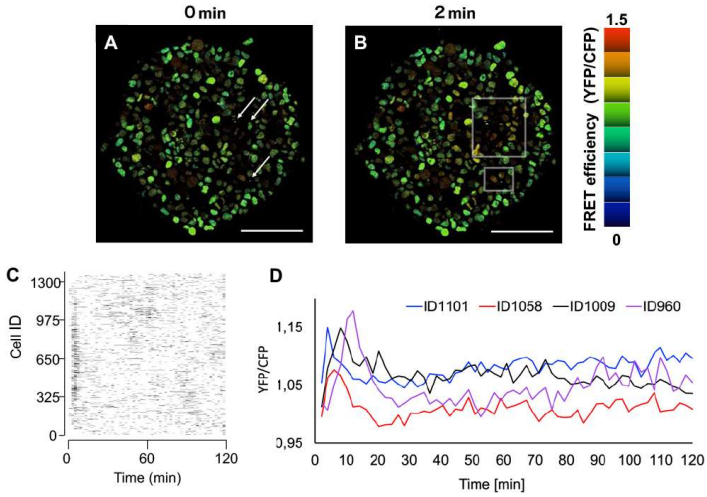

Figure 4. Ratiometric xy fluorescence images extracted from a z-stack of a #T-HeLa spheroid incubated with a reduced concentration of AuNS-Cys at 0 min (first scan, A) and 2 min after the initial scan (B), with white arrows indicating the AuNS-Cys location and white squares delimiting the heat-induced ERK activation area. Corresponding raster plot obtained from 3DeeCellTracker analysis showing the timing of ERK activation in single cells as a function of time (C). The black horizontal lines indicate the ERK-activated state, determined by the FRET efficiency of YFP/CFP exceeding the mean of the control +2 SD, and the duration of each back line is 2 min. FRET efficiency as YFP/CFP over time of three individual cells selected within the white squared area of the spheroid (D).

The raster plot obtained from 3DeeCellTracker (Figure 4C), although very similar to that observed at higher AuNS-Cys concentrations, exhibits a less pronounced activation within the first few minutes following the initial scan because of the lower concentration of AuNS-Cys used. The variation of the YFP/CFP ratio in three individual cells over time (Figure 4D), selected from the area surrounding AuNS-Cys (white squares, Figure 4B), revealed distinct sharp activation peaks occurring at different time points within the 15-min interval (maximum ratio values at 2, 8, and 12 min). These variations indicate a discrepancy in the timing of ERK activation among neighboring cells. Given that heat propagates through biological tissue at a rate of tens μm/ms,[45,46] the observed delay in ERK activation among adjacent cells is unlikely to arise from heat diffusion and instead suggests propagation of ERK signaling within the spheroid. The underlying mechanism was not directly investigated in this study. Possible explanations include paracrine signaling mediated by soluble factors, EGFR-dependent signaling cascades previously implicated in ERK activation waves, or other forms of cell–cell or mechanochemical coupling within the spheroid microenvironment.[9,47,48]

The delayed ERK activation in the neighboring cells, observed here, highlights the complexity of ERK activation, which can be triggered by both direct heat effects and secondary signaling through cell-to-cell propagation, potentially influencing cell fate. Similar patterns have been observed in studies in 2D cell monolayer where mechanical or chemical stimuli triggered wave-like ERK activation spreading across tissues.[6]

Linking heat-induced ERK activation to cell death

Investigating ERK activity in a 3D cell system under plasmon-induced heat provided valuable insights into the dynamics of ERK signaling; however, its correlation with heat-induced cell death remains to be evaluated. To this end, spheroids were incubated with a high concentration of AuNS-Cys (25 μg/mL) to ensure extensive coverage. Sulforhodamine B (SRB), a red-fluorescent marker that selectively accumulates in cells with severely compromised membranes,[49] was added to the cell culture medium as an indicator for cell death upon photothermal stimulation.

To determine the extent of photothermally induced cell death evoked by our previously set experimental conditions used for the heat-induced ERK activity experiments (Figure 2-3), control spheroids and spheroids containing AuNS-Cys were exposed to laser irradiation at 0.3 MW cm^{-2} and imaged at 0 min, 2 min, and 10 min (Figure 5A–C and D–F, respectively). At the initial scan, a low level of dead cells, appearing in red, was observed in both conditions and remained stable over the 10-min interval. This is an expected phenomenon in unperturbed spheroids, where a certain proportion of cell death naturally occurs due to limitations in nutrient and oxygen diffusion across the densely packed 3D cellular structure, leading to apoptotic and necrotic processes.[50] At this laser power, no significant increase in cell death was observed in the presence of AuNS-Cys (Figure 5D–F). Applying additional 3 s of irradiation at 4.9 MW cm^{-2} laser power prior to imaging (at 0.3 MW cm^{-2}) did not produce an immediate effect at 0 min (Figure 5G). However, after 2 min, a subset of cells underwent cell death (marked with light blue circles in Figure 5G–H), with a progressive increase over time, as additional cells exhibited cell death by 10 min (marked with green circles in Figure 5H–I). This increase in cytotoxicity can be attributed to the photothermal effect of AuNS-Cys. The cytotoxic response was even more pronounced when spheroids containing AuNS-Cys were irradiated at 14.6 MW cm^{-2} for 3 s prior to imaging. Under these conditions, a high percentage of cells exhibited cell death, as indicated by extensive red fluorescence within the spheroid structure (Figure 5J–L). The proportion of dead cells increased linearly over time, with the majority of the cells in the spheroid appearing red by 10 min post-scan (Figure 5L), demonstrating a significant photothermal-induced cytotoxic effect at this laser power. Laser-only irradiation at higher powers (14.6 MW cm^{-2} and 4.9 MW cm^{-2}) did not induce detectable cytotoxicity in the absence of AuNSs (Figure S7), indicating that the cell death observed in Figure 5G-L arise under nanoparticle-mediated photothermal conditions.

To investigate the correlation between photothermal-induced ERK activity and cell death, FRET efficiency (YFP/CFP) in #T-HeLa cells was assessed following an additional 3-s irradiation at 4.9 MW cm^{-2} prior to imaging. This laser power induced moderate levels of cell death (Figure 5G-I), whereas higher power settings (14.6 MW cm^{-2}) were not feasible due to excessive cell mortality (Figure 5J-L), which would compromise fluorescence imaging. At 4.9 MW cm^{-2}, ratiometric imaging revealed a high proportion of ERK-active cells (Figure S8), with raster plot analysis indicating that 72.2% of cells initiated ERK activity within two min from the initial scan. This activation rate was significantly higher than that observed under standard photoexcitation conditions (53.7% at 0.3 MW cm^{-2}), where no significant cell death was detected (Figure 5D-F). To exclude ERK activation induced by laser irradiation alone at a higher laser power density (4.9 MW cm^{-2}), FRET efficiency was measured in the absence of AuNS–Cys (Figure S9). Under these conditions, no ERK activation was observed, confirming that nanoparticle presence is required for the observed ERK activation and synchronization. These findings suggest that cell death within spheroids is associated with an increased proportion of ERK-active cells, corroborating the link between ERK signalling and photothermal-induced cell death.

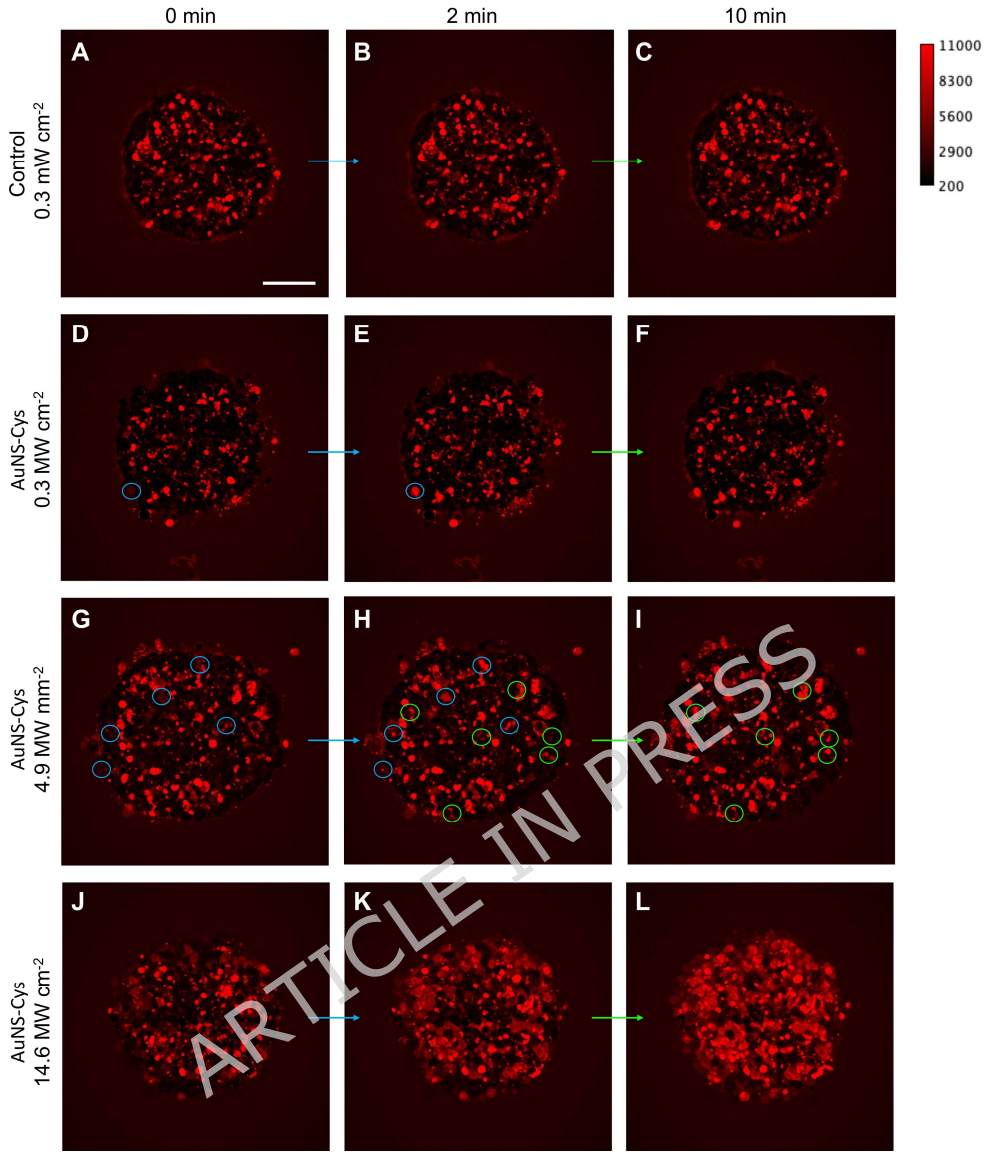

Figure 5. Spheroid cell death assay using sulforhodamine B (SRB) staining. Confocal xy fluorescence images extracted from z-stacks show #T-Hela spheroids under different conditions: control spheroids without AuNS-Cys, imaged after the first scan at 0.3 MW cm^{-2} (0 min) and at 2 min and 10 min post-scan (A–C, respectively); spheroids with AuNS-Cys, imaged after the first scan at 0.3 MW cm^{-2} (0 min) and at 2 min and 10 min post-scan (D–F, respectively); spheroids with AuNS-Cys pre-irradiated for 3 s at 4.9 MW cm^{-2}, then imaged under the same condition at 0 min, 2 min, and 10 min (G–I, respectively); spheroids with AuNS-Cys pre-irradiated for 3 s at 14.6 MW cm^{-2}, then imaged under the same condition at 0 min, 2 min, and 10 min (J-L, respectively). Scale bar: 100 μm. Two-photon excitation: 850 nm.

Furthermore, the rate of cell division under ERK experiment conditions (0.3 MW cm^{-2} laser power) was assessed over 2 h post-irradiation. Interestingly, a significant increase in cell proliferation was observed compared to steady-state conditions (control), with 102.7 ± 6.4 cell divisions recorded among 1300 cells within this period (Figure S10). This percentage was substantially higher than that of the control (74.7 ± 9.9), suggesting that at this laser power, plasmon-induced heating promotes cell division rather than cell death. Given that ERK signaling is implicated in cell proliferation and survival pathways[9,41], these results indicate an association between ERK activity and cellular fate, where laser power modulation dictates the balance between photothermal-induced death and proliferation. Despite the clear correlation between ERK activation and cellular responses, the present study does not establish a causal role for ERK signaling in determining cell fate. These insights challenge the traditional view of heat as merely destructive, instead revealing its potential as a tuneable modulator of signaling dynamics and tissue behavior**.** Recognizing this modulatory role is essential for refining nanoparticle-mediated photothermal therapy to achieve precise therapeutic outcomes while minimizing unintended cellular damage.

Conclusions

This study presents a groundbreaking approach for monitoring photothermal effects on cellular behavior within solid tumors by tracking variations in ERK signaling. By employing gold nanostars as thermal transducers, a FRET biosensor to visualize ERK activity in a 3D cell model, and the advanced deep-learning tool 3DeeCellTracker for data analysis, we have uncovered unprecedented insights into how cells within a spheroid respond to localized heat. The key findings were that (i) ERK activity occurs spontaneously and randomly in a limited number of cells within unperturbed spheroids; (ii) plasmon-induced heat drastically increases the number of ERK-activated cells; (iii) heat-induced ERK activation is synchronized among spheroid cells and occurs within a few minutes from the stimulation; (iv) heat-triggered ERK activation is shorter in duration than spontaneous activation; (v) after heat stimuli cells undergo transient ERK inactivation; (vi) ERK signals propagated several micrometers from the heat source; and (vii) the laser power used for photothermal stimulation critically determines cellular fate, influencing either proliferation or cell death.
These findings offer critical insights into the spatiotemporal dynamics of ERK signaling under photothermal conditions, providing a foundation for the rational design and optimization of next-generation cancer photothermal therapies. These findings offer critical insights into the

spatiotemporal dynamics of ERK signaling under photothermal conditions, providing a foundation for the rational design and optimization of next-generation cancer photothermal therapies. As investigating these processes in vivo remains technically challenging due to limited spatial and temporal resolution, 3D tumor models offer a powerful platform for such mechanistic studies. By advancing our understanding of how cellular behavior is modulated by heat at the molecular and multicellular levels, this study paves the way for more precise and effective thermal strategies against solid tumors.

Funding Declaration. We acknowledge financial support from MEXT under the JSPS KAKENHI (21H01753 and 21K19036 to Y.T., 22K20524 to F.T., 22K14578 and 19K15406 to M.T., JP22KK0100 to M.T., K.O., K.K., 22H02756 to K.O., 20H05669 to K.O. and T.N., 20H05669 to K.D.K., JP22H04926, 22H02625 to K.A., 21H04634, 23H04877, 23K17856 to H.U., 23H04877 to K.H. and H.U.), Bilateral Program (JPJSBP120232301 to Y.T and S.R.), Core-to-Core Program for Advanced Research Network (CCA20190003), and the Cooperative Research Program of "NJRC Mater. & Dev.", JST CREST (JPMJCR20E4 to K.O.), a grant of Joint Research by the National Institutes of Natural Sciences (01112002), Grant-in-Aid for Research at Nagoya City University (48, 1912011, 1921102), Joint Research of the Exploratory Research Center on Life and Living Systems (ExCELLS) (22EXC201, 23EXC204, 24EXC201), and Dr. H. Mitomo and Ms. C. Takeuchi for the technical support for DLS and zeta potential measurements. We acknowledge financial support from Research Foundation of Flanders (FWO) research grants (G0D4519N, G081916N, VS08523N, G0C1821N, G022724N), postdoctoral fellowship (12X1419N, 12X1423N to B.F., 12A6N25N to I.V.Z.), and from the KU Leuven (C14/15/053, C14/19/079, C14/22/085, C14/23/090). F.T. acknowledges financial support from Nakatani Foundation. We thank the Open Facility, Global Facility Center, Creative Research Institution, Hokkaido University for allowing us to use SEM and STEM. The authors would like to thank the NIKON Imaging Center at Hokkaido University for the imaging equipment and software.

Author Contributions. H.U., B.F., and T.N. conceived the idea and directed the project. F.T., Y.T., D.Y., Y.Y., M.T., and K.H. synthesized the compounds and acquired and analyzed the data. Y.T., F.T., D.Y., K.Y., M.T., K.O., S.K., M.B., I.V.Z., B.F., and S.R. performed microscopy experiments. Y.T., F.T., D.Y., B.F., and H.U. wrote the manuscript draft. F.T., D.Y., K.Y., M.T.,

C.W., K.O., K.H., J.H., K.D.K, K.A., and T.N. developed the analysis methods using the FRET sensor and deep-learning program. All the authors contributed to editing the manuscript.

Data availability

The data supporting this article have been included as part of the Supplementary Information. Supplementary information: Figure S1-10, and photothermal conversion efficiency.

Conflict of interest

The are no conflicts of interest to declare.

References

1. Bravo, M. *et al.* Nanoparticle-mediated thermal Cancer therapies: Strategies to improve clinical translatability. *Journal of Controlled Release* **372**, 751–777 (2024).
2. Zhi, D., Yang, T., O'Hagan, J., Zhang, S. & Donnelly, R. F. Photothermal therapy. *Journal of Controlled Release* **325**, 52–71 (2020).
3. Jung, H. S. *et al.* Organic molecule-based photothermal agents: an expanding photothermal therapy universe. *Chem. Soc. Rev.* **47**, 2280–2297 (2018).
4. Shen, S., Qiu, J., Huo, D. & Xia, Y. Nanomaterial-Enabled Photothermal Heating and Its Use for Cancer Therapy via Localized Hyperthermia. *Small* **20**, (2024).
5. Torii, S., Yamamoto, T., Tsuchiya, Y. & Nishida, E. ERK MAP kinase in G cell cycle progression and cancer. *Cancer Sci.* **97**, 697–702 (2006).
6. Aoki, K. *et al.* Stochastic ERK activation induced by noise and cell-to-cell propagation regulates cell density-dependent proliferation. *Mol. Cell* **52**, 529–540 (2013).
7. Courcelles, M. *et al.* Phosphoproteome dynamics reveal novel ERK1/2 MAP kinase substrates with broad spectrum of functions. *Mol. Syst. Biol.* **9**, (2013).
8. Traverse, S. *et al.* EGF triggers neuronal differentiation of PC12 cells that overexpress the EGF receptor. *Current Biology* **4**, 694–701 (1994).
9. Gagliardi, P. A. *et al.* Collective ERK/Akt activity waves orchestrate epithelial homeostasis by driving apoptosis-induced survival. *Dev. Cell* **56**, 1712-1726.e6 (2021).
10. Marshall, C. J. Specificity of receptor tyrosine kinase signaling: Transient versus sustained extracellular signal-regulated kinase activation. *Cell* **80**, 179–185 (1995).
11. Li, F. *et al.* DOX-loaded silver nanotriangles and photothermal therapy exert a synergistic antibreast cancer effect via ROS/ERK1/2 signaling pathway. *Nanotechnology* **33**, 075101 (2022).
12. Xiao, Y., Riahi, R., Torab, P., Zhang, D. D. & Wong, P. K. Collective Cell Migration in 3D Epithelial Wound Healing. *ACS Nano* acsnano.8b06305 (2019) doi:10.1021/acsnano.8b06305.
13. Darrigues, E. *et al.* 3D cultures for modeling nanomaterial-based photothermal therapy. *Nanoscale Horiz.* **5**, 400–430 (2020).
14. Anisimov, R. A., Gorin, D. A. & Abalymov, A. A. 3D Cell Spheroids as a Tool for Evaluating the Effectiveness of Carbon Nanotubes as a Drug Delivery and Photothermal Therapy Agents. *C (Basel).* **8**, 56 (2022).

15. Yuan, H. *et al.* Gold nanostars: surfactant-free synthesis, 3D modelling, and two-photon photoluminescence imaging. *Nanotechnology* **23**, 075102 (2012).
16. Ebisuya, M., Kondoh, K. & Nishida, E. The duration, magnitude and compartmentalization of ERK MAP kinase activity: mechanisms for providing signaling specificity. *J. Cell Sci.* **118**, 2997–3002 (2005).
17. Komatsu, N. *et al.* Development of an optimized backbone of FRET biosensors for kinases and GTPases. *Mol. Biol. Cell* **22**, 4647–4656 (2011).
18. Oshima, Y. *et al.* Ultrasensitive Imaging of Ca2+ Dynamics in Pancreatic Acinar Cells of Yellow Cameleon-Nano Transgenic Mice. *Int. J. Mol. Sci.* **15**, 19971–19986 (2014).
19. Oshima, A. *et al.* Two-photon microscopic analysis of acetylcholine-induced mucus secretion in guinea pig nasal glands. *Cell Calcium* **37**, 349–357 (2005).
20. Schindelin, J. *et al.* Fiji: an open-source platform for biological-image analysis. *Nat. Methods* **9**, 676–682 (2012).
21. Wen, C. & Kimura, K. Tracking Moving Cells in 3D Time Lapse Images Using 3DeeCellTracker. *Bio. Protoc.* **12**, 1–12 (2022).
22. Wen, C. *et al.* 3DeeCellTracker, a deep learning-based pipeline for segmenting and tracking cells in 3D time lapse images. *Elife* **10**, (2021).
23. Çiçek, Ö., Abdulkadir, A., Lienkamp, S. S., Brox, T. & Ronneberger, O. 3D U-Net: Learning Dense Volumetric Segmentation from Sparse Annotation. *Lecture Notes in Computer Science (including subseries Lecture Notes in Artificial Intelligence and Lecture Notes in Bioinformatics)* **9901 LNCS**, 424–432 (2016).
24. Gao, N. *et al.* Shape-Dependent Two-Photon Photoluminescence of Single Gold Nanoparticles. *The Journal of Physical Chemistry C* **118**, 13904–13911 (2014).
25. Guo, J., Zhang, Y., Luo, Y., Shen, F. & Sun, C. Efficient fluorescence resonance energy transfer between oppositely charged CdTe quantum dots and gold nanoparticles for turn-on fluorescence detection of glyphosate. *Talanta* **125**, 385–392 (2014).
26. Fernandes, F., Talukdar, I. & Kowshik, M. Cysteamine functionalized gold nanoparticles exhibit high efficiency delivery of genetic materials in embryonic stem cells majorly via clathrin mediated endocytosis. *Int. J. Pharm.* **667**, 124928 (2024).
27. Becerril-Castro, I. B. *et al.* Gold Nanostars: Synthesis, Optical and SERS Analytical Properties. *Analysis & Sensing* **2**, (2022).
28. Schild, H. G., Muthukumar, M. & Tirrell, D. A. Cononsolvency in Mixed Aqueous Solutions of Poly(N- isopropylacrylamide). *Macromolecules* **24**, 948–952 (1991).
29. Sasikumar, D., Takano, Y. & Biju, V. Photoinduced Betaine Generation for Efficient Photothermal Energy Conversion. *Chemistry – A European Journal* **26**, 2060–2066 (2020).
30. Vikas, Kumar, R. & Soni, S. Concentration-dependent photothermal conversion efficiency of gold nanoparticles under near-infrared laser and broadband irradiation. *Beilstein Journal of Nanotechnology 14:20* **14**, 205–217 (2023).
31. Hirashima, T. Live imaging approach of dynamic multicellular responses in ERK signaling during vertebrate tissue development. *Biochemical Journal* **479**, 129–143 (2022).
32. Xin, T. *et al.* Oncogenic Kras induces spatiotemporally specific tissue deformation through converting pulsatile into sustained ERK activation. *Nature Cell Biology 2024 26:6* **26**, 859–867 (2024).
33. Nishino, M. *et al.* Measurement and visualization of cell membrane surface charge in fixed cultured cells related with cell morphology. *PLoS One* **15**, e0236373 (2020).
34. Behzadi, S. *et al.* Cellular Uptake of Nanoparticles: Journey Inside the Cell. *Chem. Soc. Rev.* **46**, 4218 (2017).

35. Liu, S. *et al.* An Inhalable Spike–Conjugated Gold Nanoparticle for Treating Acute Lung Inflammation. *Adv. Funct. Mater.* e15906 (2025) doi:10.1002/ADFM.202515906.
36. Lee, L. K. C. *et al.* Small Gold Nanoparticles Alleviate Huntington's Disease via Modulating p38α Mitogen-Activated Protein Kinase and Pyruvate Dehydrogenase Kinase 1. *ACS Nano* **20**, 683–699 (2026).
37. Chan, C. K. W. *et al.* A sub-10-nm,folic acid-conjugated gold nanoparticle as self-therapeutic treatment of tubulointerstitial fibrosis. *Proc. Natl. Acad. Sci. U. S. A.* **120**, (2023).
38. Arvizo, R. R. *et al.* Inhibition of tumor growth and metastasis by a self-therapeutic nanoparticle. *Proc. Natl. Acad. Sci. U. S. A.* **110**, 6700–6705 (2013).
39. Cao, J. Laser Pulse Duration Optimization for Photothermal Therapy with Gold Nanostars. *Int. J. Med. Phys. Clin. Eng. Radiat. Oncol.* **07**, 391–402 (2018).
40. Beucher, S. & Meyer, F. The Morphological Approach to Segmentation: The Watershed Transformation. *Mathematical Morphology in Image Processing* 433–481 (2019) doi:10.1201/9781482277234-12.
41. Sugiura, R., Satoh, R. & Takasaki, T. ERK: A Double-Edged Sword in Cancer. ERK-Dependent Apoptosis as a Potential Therapeutic Strategy for Cancer. *Cells* **10**, (2021).
42. Jaque, D. *et al.* Nanoparticles for photothermal therapies. *Nanoscale* **6**, 9494–9530 (2014).
43. Wilson, M. Z., Ravindran, P. T., Lim, W. A. & Toettcher, J. E. Tracing Information Flow from Erk to Target Gene Induction Reveals Mechanisms of Dynamic and Combinatorial Control. *Mol. Cell* **67**, 757-769.e5 (2017).
44. Blumenberg, M. Profiling and metaanalysis of epidermal keratinocytes responses to epidermal growth factor. *BMC Genomics* **14**, (2013).
45. El-Brawany, M. A. *et al.* Measurement of thermal and ultrasonic properties of some biological tissues. *J. Med. Eng. Technol.* **33**, 249–256 (2009).
46. Kim, D. & Kim, H. Analysis of Optimal Treatment Starting Time for Photothermal Therapy Through Analysis of Diffusion Behavior of Gold Nanoparticles. *Int. J. Nanomedicine* **19**, 3167 (2024).
47. Hino, N. *et al.* ERK-Mediated Mechanochemical Waves Direct Collective Cell Polarization. *Dev. Cell* **53**, 646-660.e8 (2020).
48. Lin, S. *et al.* Redundant roles of EGFR ligands in the ERK activation waves during collective cell migration. *Life Sci. Alliance* **5**, (2022).
49. Nishimura, Y. & Lemasters, J. J. Glycine blocks opening of a death channel in cultured hepatic sinusoidal endothelial cells during chemical hypoxia. *Cell Death & Differentiation 2001 8:8* **8**, 850–858 (2001).
50. Ohori-Morita, Y., Ashry, A., Niibe, K. & Egusa, H. Current perspectives on the dynamic culture of mesenchymal stromal/stem cell spheroids. *Stem Cells Transl. Med.* https://doi.org/10.1093/STCLTM/SZAE093 (2024) doi:10.1093/STCLTM/SZAE093.

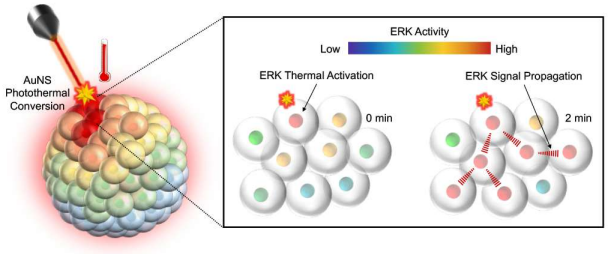

TOC